Pore-scale direct numerical simulation of particle transport in porous media

Junwei Su[1], Guoliang Chai[1], Le Wang[2], Weidong Cao[3], Zhaolin Gu[1],
Chungang Chen[4*], Xiao Yun Xu[5]

[1] School of Human Settlement and Civil Engineering, Xi'an Jiaotong University, Xi'an, 710049, China;

[2] Mechanical Engineering College, Xi'an Shiyou University, Xi'an, 710049, China;

[3] Research Institute of Exploration and Development, Shengli Oilfield Company, Sinopec group, Dongying, 257015, China;

[4] School of Aerospace & State Key Laboratory for Strength and Vibration of Mechanical Structures, Xi'an Jiaotong University, Xi'an 710049, China; cgchen@mail.xjtu.edu.cn

[5] Department of Chemical Engineering, Imperial College London, London SW7 2AZ, UK.

Abstract: A computational platform for direct numerical simulation of fluid-particle two-phase flow in porous media is presented in this study. In the proposed platform, the Navier-Stokes equations are used to describe the motion of the continuous phase, while the discrete element method (DEM) is employed to evaluate particle-particle and particle-wall interactions, with a fictitious domain method being adopted to evaluate particle-fluid interactions. Particle-wall contact states are detected by the ERIGID scheme. Moreover, a new scheme, namely, base point-increment method is developed to improve the accuracy of particle tracking in porous media. In order to improve computationally efficiency, a time splitting strategy is applied to couple the fluid and DEM solvers, allowing different time steps to be used which are adaptively determined according to the stability conditions of each solver. The proposed platform is applied to particle transport in a porous medium with its pore structure being reconstructed from micro-CT scans from a real rock. By incorporating the effect of pore structure which has a comparable size to the particles, numerical results reveal a number of distinct microscopic flow mechanisms and the corresponding macroscopic characteristics. The time evolution of the inlet to outlet pressure-difference consists of large-scale spikes and small-scale fluctuations. Apart from the influence through direct contacts between particles, the motion of a particle can also be affected by particles without contact through blocking a nearby passage for fluid flow. Particle size has a profound influence on the macroscopic motion behavior of particles. Small particles are easier to move along the main stream and less dispersive in the direction perpendicular to the flow than large particles.

Keywords: Fluid-Particle Flow; Pore Scale; Fictitious Domain Method; Discrete Element

Method.

1. Introduction

Particle transport in porous media plays an important role in many engineering fields, for instance, viscoelastic particle flooding in enhanced oil recovery [1], leaching mining [2], coal bed gas mining [3], sand production in oil recovery [4], particle removal by filtration for water treatment [5-8], and drug delivery [9]. Investigation of fluid-particle dynamics in porous media is of uttermost importance to understand the migration behavior of particles, which is the basis for manual control of the migration process of particle cloud in a porous medium. To study particle transport in porous media, existing methods mainly include macroscopic-scale simulations using convection-diffusion equation [10] and experimental research in the field of microfluidics [11]. Macroscopic-scale simulations can predict the macroscopic movement and dispersion of particles, but ignore the effect of detailed pore structure or particle properties. Also, accurate evaluation of transport parameters (e.g. diffusion coefficient, convection velocity) remains a significant challenge. Experimental studies of particle migration in porous media allow direct observation of the transport process of particles in porous media [11]. However, such experimental studies cannot reveal the mechanical characteristics of fluid-particle interactions in the pores, nor can they quantify the effect of pore structure and particle properties on particle motion. In this study, a coupled computational fluid dynamics (CFD) and discrete element method (DEM) method is proposed for direct tracking of particles in a porous medium, which explicitly solves fluid-particle and particle-particle interactions.

Discrete element method, which was first introduced by Cundall and Strack as a useful tool to simulate particle interactions [12], has now been applied in many fields involving particle motions, especially in the study of fluidized beds in chemical engineering [13,14], energy industry and other industrial processes [15-20] In a DEM model, particle-particle contact forces and particle-wall contact forces, including elastic, viscous and sliding forces, are described using simple mechanical elements, such as springs, dash dots and sliders. The well-established Newton's second law is used to govern the motion of particles under the Lagrangian framework. This method can provide particle-scale information, such as particle trajectories and mechanical characteristics of each particle, which are difficult or impossible to be obtained using macroscopic simulation methods. In the meanwhile, the macroscopic behavior of particle clouds is derived through the evaluation of interactions between individual particles as well as those between particles and their surrounding fluids and walls [15]. DEM offers a very effective tool to understand particle behaviors in porous media by directly calculating all the relevant interactions, thereby providing the basis for accurate control of particle transport.

A CFD-DEM coupled method has been applied to simulate particle transport in a porous medium [21], with a new algorithm developed to detect collisions between the particles and pore walls [21-23]. The drag force model based on the point source assumption was adopted, requiring

the size of the particle to be much smaller than that of the mesh cell [19]. Therefore, this method is not suitable for the present study, since the particles concerned here have a similar size to the pore channel. To overcome this difficulty, direct numerical simulation (DNS) techniques, such as fictitious domain method [24, 25] or immersed boundary method [26, 27], can be adopted to evaluate the interaction between fluid and particles. Although a CFD-DNS-DEM coupled model has been applied to particle flows [28, 29], the application of such methods in microscopic simulation of pore-scale particle flows is still intractable mainly due to the unique physical features and complex flow phenomena in pore space. So far, direct numerical simulations of particle flow at the pore-scale are rarely reported. To develop a feasible numerical method for pore-scale particle flow simulations, more efforts must be made to address the following issues:

(1) Fast determination of the computational cells covered by a particle in an arbitrarily polyhedral mesh;
(2) Fast determination of contact states between particles and arbitrarily complex walls;
(3) Accurate and efficient evaluation of the fluid-particle interaction force;
(4) Accurate calculation of the cumulative effect of particle clogging on particle-particle or particle-wall overlap;
(5) Efficient time integration to ensure the stability and computational efficiency of a system with highly fluctuating velocities.

The numerical model proposed in this study adopts the following techniques to overcome the above difficulties.

(1) To find the computational cells covered by a particle, we first use the point locating algorithm [30, 31] to find the cell where the center of a particle is located, and then find all the cells covered by the particle through nearby-cell searching according to the cell neighbor relation and particle radius.
(2) Several new methods have been developed for determination of the contact state between a particle and the wall [21-23, 32-33]. The ERIGID algorithm [21] is adopted in this study as it offers a good overall performance in computational accuracy and efficiency.
(3) A fictitious domain method is used to evaluate the fluid-particle interaction force for its simplicity and good accuracy [24].
(4) When particles enter a throat, they will slow down due to the damping force from the pore wall. Considering a very small time-step, the displacement of a particle can be rather small and may reach the machine precision within a single time step. As a result, the accuracy of updating of particle location and evaluation of particle overlap will be obviously degraded during the simulation. In this study, we propose a new method, namely base point-increment method, to solve this problem.
(5) When a particle clogs a throat, the local upstream pressure will increase sharply and flow in the neighbor channels will accelerate. Whereas when a particle breaks through a throat, the upstream pressure will suddenly drop and flow in the neighbor channels will

decelerate. As a result, fluid velocity in the pore channels may experience high levels of fluctuation, rending the simulation unstable or inefficient with a fixed time step. Therefore, a variable time-stepping scheme is necessary for the CFD-DNS-DEM coupled model in this study.

The paper is organized as follows. The mathematical model is described in section 2, which includes dynamic models for the two phases, the fictitious domain method for solving fluid-particle interactions, the base-point increment method for improving the accuracy of DEM solver and the new time integration strategy for assuring computational efficiency and stability. A number of test cases are described in section 3 to validate the proposed model. Numerical simulations of fluid-particle flow in a realistic rock are presented in section 4, along with discussions on the mechanisms of fluid-particle flow in porous media. Finally, a short summary and conclusions are given in section 5.

2. Mathematical Model

The solution domain Ω contains the fluid covered zone Ω_f and particle covered zone Ω_s, which satisfies $\Omega=\Omega_f \cup \Omega_s$. Γ_s is the boundary of particle covered zone. The solution domain may contain several discontinuous solid particle zones. For instance, particle i covers zone Ω_{pi}, and the boundary between the particle and fluid is Γ_{pi}. The fluid is a viscous incompressible Newton fluid with a density of ρ_f and a viscosity of μ.

2.1 Continuous phase hydrodynamics

Navier-Stokes equation is employed to describe the fluid motion in the fluid domain in the Eulerian Framework

$$\rho_f \frac{\partial \mathbf{u}}{\partial t} + \rho_f \nabla \cdot (\mathbf{u}\mathbf{u}) - \nabla \cdot \boldsymbol{\tau} = 0 \tag{1}$$

where, $\mathbf{u}$ is fluid velocity and t is time. $\boldsymbol{\tau}$ is stress tensor of the fluid given by

$$\boldsymbol{\tau} = -p\mathbf{I} + \mu(\nabla \mathbf{u} + \nabla \mathbf{u}^T) \tag{2}$$

p is pressure and $\mathbf{I}$ is a unit tensor. The continuity equation describing the mass conservation and incompressible constraint is

$$\nabla \cdot \mathbf{u} = 0 \tag{3}$$

2.2 Particle dynamics

In this work, each particle in the system is tracked using Newton' s second Law in the Lagrangian framework, according to

$$\mathbf{F}_i = \sum_j \mathbf{F}_{ij}^{p-p} + \sum_w \mathbf{F}_{iw}^{w-p} + \mathbf{F}_i^{f-p} + m\mathbf{g} \tag{4}$$

where $\mathbf{F}_i$ is the total force acting on particle i, $\mathbf{F}_{ij}^{p-p}$ and $\mathbf{F}_{iw}^{w-p}$ are the forces acting on particle i

by particle j and wall, respectively. $\mathbf{F}_i^{f-p}$ is the fluid force acting on particle i, evaluated using fictitious domain method presented in the next section. m is particle mass, $\mathbf{g}$ is gravity acceleration. The sum of the first and second terms on the right-hand side represents collision induced force, denoted as $\mathbf{F}^c$ in later discussion.

For particle torque, the following relation is satisfied

$$\mathbf{T}_i = \sum_j \mathbf{r}_{ic} \times \mathbf{F}_{ij}^{p-p} + \sum_w \mathbf{r}_{ic} \times \mathbf{F}_{iw}^{w-p} + \mathbf{T}_i^{f-p} \tag{5}$$

where $\mathbf{r}_{ic}$ is a vector from the center of particle i to the contact point. The summation of the first and second terms is collision induced torque, denoted as $\mathbf{T}^c$ in later discussion.

2.2.1 Discrete Element Method

Discrete element method is employed to evaluate particle-particle (or particle-wall) contact forces. According to Cundall and Strack [12], the normal component of the contact force, $\mathbf{F}_{nij}^{p-p}$ for particle-particle contact is

$$\mathbf{F}_{nij}^{p-p} = (-k_n\delta_n - \eta_n\mathbf{V}_{ij}\cdot\mathbf{n})\mathbf{n} \tag{6}$$

and $\mathbf{F}_{niw}^{w-p}$ for particle-wall contact is

$$\mathbf{F}_{niw}^{w-p} = (-k_{nw}\delta_{nw} - \eta_n\mathbf{V}_{iw}\cdot\mathbf{n}_w)\mathbf{n}_w \tag{7}$$

The tangential component of contact force, $\mathbf{F}_{tij}^{p-p}$ particle-particle interaction is

$$\mathbf{F}_{tij}^{p-p} = -k_t\boldsymbol{\delta}_t - \eta_t\mathbf{V}_{tij} \tag{8}$$

and $\mathbf{F}_{tiw}^{w-p}$ for particle-wall interaction is

$$\mathbf{F}_{tiw}^{w-p} = -k_{tw}\boldsymbol{\delta}_{tw} - \eta_{tw}\mathbf{V}_{tiw} \tag{9}$$

where k_n(k_{nw}) and η_n(η_{nw}) are the stiffness coefficient and damping coefficient, respectively, for particle-particle (or particle-wall) interactions in the normal direction. k_t(k_{tw}) and η_t (η_{tw}) are those in the tangential direction. $\delta_{n(w)}$ is particle-particle (or particle-wall) overlap in the normal direction. $\boldsymbol{\delta}_{t(w)}$ is particle-particle (or particle-wall) displacement in the tangential direction. $\mathbf{V}_{ij}$ ($\mathbf{V}_{iw}$) is the velocity of particle i relative to particle j (or wall), $\mathbf{n}_w$ is the vector pointing from the center of particle i to that of particle j (or the contact point on wall).

If the tangential force and the normal force satisfy the following relation

$$\left|\mathbf{F}_{tij(w)}^{p(w)-p}\right| \geq \chi\left|\mathbf{F}_{nij(w)}^{p(w)-p}\right| \tag{10}$$

the particles (or particle-wall) in contact will slide against each other, and the tangential force is given as

$$\mathbf{F}_{tij(w)}^{p(w)-p} = -\chi\left|\mathbf{F}_{nij(w)}^{p(w)-p}\right|\frac{\boldsymbol{\delta}_{t(w)}}{|\boldsymbol{\delta}_{t(w)}|} \tag{11}$$

where χ is the frictional coefficient.

A more elaborate description of the discrete element model can be found in our previous work [22]. Determination of the physical parameters, such as stiffness coefficient and damping coefficient, can be found in Tsuji et al [34].

Efficiency of contact detection for particle-particle interaction and particle-wall interaction is essentially important for the computational loads in discrete element simulation. In this work, No-Binary-Search (NBS) algorithm is employed to find candidate contact spheres for each sphere in the system [35]. Initially, a background mesh including continuous and non-overlapped cubes is created according to the following relation

$$(\mathrm{dx}, \mathrm{dy}, \mathrm{dz}) = \left(\left(\frac{Dx}{int\left(\frac{Dx}{d_{max}}\right)} \right), \left(\frac{Dy}{int\left(\frac{Dy}{d_{max}}\right)} \right), \left(\frac{Dz}{int\left(\frac{Dz}{d_{max}}\right)} \right) \right) \tag{12}$$

where, dx, dy and dz are size of the cubes in x, y and z direction. Dx, Dy and Dz are size of the bound box of the solution domain. d_{max} is the diameter of the biggest particle. $int(x)$ returns the biggest integer less than x. Particles are filled into cubes using the following relation

$$(i, j, k) = \left(int\left(\frac{p_x - D_{min,x}}{dx}\right), int\left(\frac{p_y - D_{min,y}}{dy}\right), int\left(\frac{p_z - D_{min,z}}{dz}\right) \right) \tag{13}$$

Where $D_{min,x}$, $D_{min,y}$ and $D_{min,z}$ are the smallest coordinates of the bound box of the solution domain in x, y and z direction. (p_x, p_y, p_z) is the particle location. The particles in cubes ([i-1, i+1], [j-1, j+1], [k-1, k+1]) are the potential contact pairs for particles in cube (i, j, k). Efficient RIGID (ERIGID) algorithm [21] is used to detect the contact states between spheres and pore walls.

2.2.2 Enhance DEM accuracy for pore-scale simulation

Particle flow in a porous medium may involve many unique microscopic flow phenomena and macroscopic flow behaviors. Accurate capture of these phenomena and behaviors is critically important for investigating pore scale fluid-particle motion characteristics. Due to variations in particle size, particle flow simulation programs designed for macroscopic flow would encounter some problems when applied to pore scale simulations (e.g. the position of slowly moving particle remains stationary; spurious currents in particle-contact force evaluation). It is found that all these problems are related to errors in evaluating particle positions, although similar problems also exist but not as serious in macroscopic particle flow simulations. These are explained in detail below.

Consider two particles with a radius r, located at $x_p - r$ and $x_p + r$ at a given time point, they collide with each other at a velocity of v_1 and v_2, respectively. After a time-interval of Δt, the two particles move to $x_p - r + v_1\Delta t$ and $x_p + r - v_2\Delta t$. The overlap between them should be $2r - |(x_p - r + v_1\Delta t) - (x_p + r - v_2\Delta t)| = (v_1 + v_2)\Delta t$. In the discrete element method, in order to track the complete process of all collisions, the required time step Δt is usually very small. As a result, the spatial coordinate $x_p - r$ ($x_p + r$) of the particle is much larger than the distance $v_1\Delta t$ ($v_2\Delta t$) the particle travels within a time step Δt (which is proportional to $r^{3/2}$). In macroscopic scale flow simulations, the particle size is relatively large, and the difference between a particle's location coordinate and particle motion distance within a time step is manageable using double precision variables. However, in pore scale flows, the particle size is much smaller (100 μm in the present study), the corresponding time step is small ($< 1\times10^{-6}$ s), and particle velocity is very low (for

example: 0.001 m/s). Within a time-step, the particle travel distance is about 1×10^{-9} m, which is several orders of magnitude smaller than the location coordinate of the particle $x_p \pm r$. Hence, the updated particle location $x_p \pm r + v_1 \Delta t$ is almost the same as $x_p \pm r$ (also known as "a large number annihilating a small number"). As a result, the position of the particle remains unchanged. If there is a congestion of particles in the throat, their velocities drop (for example less than 10^{-4} m/s), so that the particle travelling distance within a time step becomes even smaller (10^{-10} m). Such an ultra-small displacement is almost undetectable on the macroscopic scale, causing particles to become 'stuck', thus affecting the motion of the continuous fluid phase and further influencing the migration and dispersion of particles in space. In addition, the accuracy of inter-particle overlap can be seriously affected by the inaccuracy in particle location, which will further affect particle movement.

To avoid the problems caused by "a large number annihilating a small number" when updating particle location, in this paper, we describe the location of the particle using a compound structure, whereby the location of particle is described by a base point $\mathbf{x}_{base}$ and a tiny increment $\mathbf{x}_{inc}$ on the base point, and is recorded as ($\mathbf{x}_{base}$, $\mathbf{x}_{inc}$). This method is named as base point-increment (BPI) method hereinafter. In this BPI method, the particle location and the inter-particle overlap are evaluated according to

(1) for the particle location

$$(\mathbf{x}_{base}, \mathbf{x}_{inc}) + \mathbf{v}\Delta t = (\mathbf{x}_{base}, \mathbf{x}_{inc} + \mathbf{v}\Delta t) \tag{14}$$

(2) for the overlap between particles *a* and *b*

$$\delta_{ab} = \left|\left[(r_a + r_b)\mathbf{n} - (\mathbf{x}^a_{base} - \mathbf{x}^b_{base})\right] - \left(\mathbf{x}^a_{inc} - \mathbf{x}^b_{inc}\right)\right| \tag{15}$$

where ,

$$\mathbf{n} = \frac{(\mathbf{x}^a_{base} - \mathbf{x}^b_{base}) + (\mathbf{x}^a_{inc} - \mathbf{x}^b_{inc})}{|(\mathbf{x}^a_{base} - \mathbf{x}^b_{base}) + (\mathbf{x}^a_{inc} - \mathbf{x}^b_{inc})|} \tag{16}$$

The compound structure is refreshed every several time steps according to

$$(\mathbf{x}_{base}, \mathbf{x}_{inc}) = \begin{cases} (\mathbf{x}_{base} + \mathbf{x}_{inc}, 0) & for\ \mathbf{x}_{base} \le 10^4 \mathbf{x}_{inc} \\ (\mathbf{x}_{base}, \mathbf{x}_{inc}) & for\ \mathbf{x}_{base} > 10^4 \mathbf{x}_{inc} \end{cases} \tag{17}$$

The BPI method enables the particle location and inter-particle overlap to be evaluated with high accuracy, thereby enhancing the accuracy in the simulation of fluid-particle in a porous medium.

2.3 Fictitious Domain Method for Fluid-Particle Interaction

The core idea of the fictitious domain method is to add a force in the solid domain to make the fluid behave like a solid. As a result, Navier-Stokes equation can be applied to the whole solution domain, which is given by [24]

$$\rho_f \frac{\partial \mathbf{u}}{\partial t} + \rho_f \nabla \cdot (\mathbf{u}\mathbf{u}) - \nabla \cdot \boldsymbol{\tau} = \rho_f \boldsymbol{\lambda} \tag{18}$$

where $\boldsymbol{\lambda}$ is a force acting on the fluid inside the particle covered zone to enforce the rigid body condition. This force only exists in particle covered zone and is zero elsewhere. According to

Equations (4), (5) the following equations are satisfied for particle translation

$$m\frac{d\mathbf{V}}{dt} = \mathbf{F}^{hyd} + \left(1 - \frac{\rho_f}{\rho_p}\right)m\mathbf{g} + \mathbf{F}^{c} \tag{19}$$

and for particle rotation

$$\mathbf{J}\frac{d\boldsymbol{\omega}}{dt} + \boldsymbol{\omega} \times (\mathbf{J} \cdot \boldsymbol{\omega}) = \mathbf{T}^{hyd} + \mathbf{T}^{c} \tag{20}$$

where $\mathbf{V}$ and $\boldsymbol{\omega}$ are particle translation velocity and rotation velocity, respectively. $\mathbf{J}$ is particle moment of inertia. $\mathbf{F}^{hyd}$ and $\mathbf{T}^{hyd}$ are hydrodynamic force and torque, expressed as

$$\mathbf{F}^{hyd} = \int_{\Gamma_s} \mathbf{n} \cdot \boldsymbol{\tau} \mathrm{d}S \tag{21}$$

$$\mathbf{T}^{hyd} = \int_{\Gamma_s} \mathbf{r} \times (\mathbf{n} \cdot \boldsymbol{\tau}) \mathrm{d}S \tag{22}$$

$\mathbf{n}$ is the normal vector pointing out of the particle solid boundary, and $\mathbf{r}$ is the location vector.

The integration of equation (18) in particle covered domain is as follows.

$$\frac{\rho_f}{\rho_p}m\frac{d\mathbf{V}}{dt} - \int_{\Omega_p} \nabla \cdot \boldsymbol{\tau} d\mathbf{x} = \int_{\Omega_p} \boldsymbol{\lambda} d\mathbf{x} \tag{23}$$

The first term on the left-hand side of Equation (23) is the integration of unsteady term and convection term of Equation (18). According to Gaussian theorem, the second term on the left-hand side of equation (23) is equivalent to the term on the right-hand side of equation (21), so that equation (23) can be written as

$$\mathbf{F}^{hyd} = \frac{\rho_f}{\rho_p}m\frac{d\mathbf{V}}{dt} - \int_{\Omega_p} \boldsymbol{\lambda} d\mathbf{x} \tag{24}$$

similarly, the hydrodynamics moment is written as

$$\mathbf{T}^{hyd} = \frac{\rho_f}{\rho_p}\left[\mathbf{J}\frac{d\boldsymbol{\omega}}{dt} + \boldsymbol{\omega} \times (\mathbf{J} \cdot \boldsymbol{\omega})\right] - \int_{\Omega_p} \mathbf{r} \times \boldsymbol{\lambda} d\mathbf{x} \tag{25}$$

Equations (3), (18), (19), (20), (24) and (25) constitute the set of mechanical equations for direct numerical simulation of particle flow in porous media.

2.4 Solution Method

2.4.1 Fluid subproblem

It would be desirable to adopt an unstructured mesh for pore scale simulations. In this work, arbitrarily polyhedral finite volume method in an open source CFD package OpenFOAM is employed to discretize Navier-Stokes Equation [36] and PISO algorithm is used to decouple the momentum and continuity equations [37]. The semi-discretization form of Equation (18) can be written as

$$a_p\mathbf{u} = \mathbf{A}_H - \nabla p \tag{26}$$

where a_p is the diagonal coefficient in coefficient matrix discretized from Equation (18), and $\mathbf{A}_H$ is written as

$$\mathbf{A}_H = \sum_N a_N\mathbf{u} + \boldsymbol{b} \tag{27}$$

a_N is the implicit contribution coefficient of neighbor cells to the cell concerned. b includes all the explicit discretization contributions except pressure. Because $\boldsymbol{\lambda}$ at the next step is unknown at this stage and explicit treatment is generally applied.

Equation (26) can be transformed to the following form

$$\mathbf{u} = \frac{\mathbf{A}_{\mathrm{H}}}{a_p} - \frac{\nabla p}{a_p} \tag{28}$$

Equation (28) should satisfy the continuity equation. However, this equation is the velocity relation at the cell center when applied to continuity equation, it is assumed that the above equation is also satisfied at the face center (Rhoe-Chow interpolation [38]), i.e.

$$\mathbf{u}_f = \frac{(\mathbf{A}_{\mathrm{H}})_f}{(a_p)_f} - \frac{(\nabla p)_f}{(a_p)_f} \tag{29}$$

Substitution of Equation (29) to Equation (3) yields

$$\nabla \cdot \left(\frac{1}{a_p}\nabla p\right) = \nabla \cdot \left(\frac{(\mathbf{A}_{\mathrm{H}})_f}{(a_p)_f}\right) \tag{30}$$

Equation (30) is the pressure equation derived from PISO algorithm. Once the new pressure is obtained using this equation, velocity at the cell center and that at the face center are updated using Equation (28) and Equation (29) explicitly.

2.4.2 Particle subproblem

Rigid body constraint in particle covered zone is not satisfied after solving the fluid domain, this is caused by the fact that we treat $\boldsymbol{\lambda}$ in Equation (18) in an explicit manner. For particle covered zone, the following relation should be satisfied

$$\tilde{\mathbf{u}}^{n+1} = \mathbf{V}^{n+1} + \boldsymbol{\omega}^{n+1} \times \mathbf{r} \qquad \mathbf{x} \in \Omega_p \tag{31}$$

where $\tilde{\mathbf{u}}^{n+1}$is the fluid velocity satisfying the rigid body constraint, $\mathbf{r}$ is the vector from particle center to a location in the particle covered zone.

With $\boldsymbol{\lambda}^{\mathbf{n}}$, the discretized form of Equation (18) can be written as

$$\frac{\mathbf{u}^{n+1}-\mathbf{u}^n}{\Delta t} = \boldsymbol{\mathcal{F}} + \boldsymbol{\lambda}^n \tag{32}$$

With $\boldsymbol{\lambda}^{\mathbf{n+1}}$, the discretized form of Equation (18) can be written as

$$\frac{\tilde{\mathbf{u}}^{n+1}-\mathbf{u}^n}{\Delta t} = \tilde{\boldsymbol{\mathcal{F}}} + \boldsymbol{\lambda}^{n+1} \tag{33}$$

$\boldsymbol{\mathcal{F}}$ and $\tilde{\boldsymbol{\mathcal{F}}}$ are discretization of convection and diffusion terms, respectively. Subtraction of Equation (32) from Equation (33) yields

$$\lambda^{n+1} = \frac{\tilde{\mathbf{u}}^{n+1}-\mathbf{u}^{n+1}}{\Delta t} + \tilde{\boldsymbol{\mathcal{F}}} - \boldsymbol{\mathcal{F}} - \boldsymbol{\lambda}^n \tag{34}$$

The second and third items on the right-hand side of Equation (34) are the differences between the convective and diffusive effects before and after correction. $\tilde{\boldsymbol{\mathcal{F}}}$ is dependent on $\boldsymbol{\lambda}^{n+1}$. The deferred correction method can be employed to improve the evaluation accuracy of $\boldsymbol{\lambda}$. However, for the sake of simplicity, such a difference is neglected in this work. As a result, Equation (34) can be rewritten as

$$\boldsymbol{\lambda}^{n+1} = \frac{\tilde{\mathbf{u}}^{n+1}-\mathbf{u}^{n+1}}{\Delta t} - \boldsymbol{\lambda}^n \tag{35}$$

Substitution of Equation (35) into Equations (19) and (20) yields

$$m\mathbf{V}^{n+1} = \frac{\rho_p-\rho_f}{\rho_p} m(\mathbf{V}^n + \mathbf{g}\Delta t) + \rho_f \int_{\Omega_p} (\mathbf{u}^{n+1} - \lambda^n) d\mathbf{x} + \mathbf{F}^c \Delta t \tag{36}$$

$$\mathbf{J}\cdot\boldsymbol{\omega}^{n+1} = \frac{\rho_p-\rho_f}{\rho_p}(\mathbf{J}\cdot\boldsymbol{\omega}^n - \boldsymbol{\omega}^n \times (\mathbf{J}\cdot\boldsymbol{\omega}^n)\Delta t) + \rho_f \int_{\Omega_p} \mathbf{r} \times (\mathbf{u}^{n+1} - \lambda^n) d\mathbf{x} + \mathbf{T}^c \Delta t \tag{37}$$

The particle velocity and angular velocity can be tracked by Equation (36) and Equation (37).

The two equations contain the integral of the physical quantity in the particle covered zone. Because the grid face and the surface of particles do not fit in the solution process, the approximated Heaviside function is used when evaluating the integration

$$\int_{\Omega_p} \Phi d\mathbf{x} = \int_{D(\Omega_p)} I(\mathbf{x}) \Phi d\mathbf{x} \tag{38}$$

where $D(\Omega_p)$ is a solution domain containing Ω_p. $I(x)$ is an indicator function, expressed as

$$I(x) = 1 - H(\psi(\mathbf{x})) \tag{39}$$

where $\psi(\mathbf{x})$ is the distance between position $\mathbf{x}$ and particle center, which is negative inside the particle and positive outside the particle. The approximate Heaviside function can be expressed as

$$H(s) = \frac{1}{2}\left(1 + \tanh(b\frac{s}{\Delta})\right) \tag{40}$$

b is smooth length and b=5 is adopted in this work. Δ is mesh size.

2.4.2 Eulerian-Lagrangian coupling

In the method described in this work for direct numerical simulation of particle flow in porous media, we use Navier-Stokes Equation to describe the continuous phase, DEM-based Lagrangian method to describe particle dynamics, and fictitious domain method for fluid-particle interaction. Since two different physical quantities are coupled in the algorithm, these should be treated with caution.

The first physical quantity is velocity. Solved using Equations (36) and (37), particle velocity should be mapped to particle covered zone in Eulerian framework. For cells completely covered by the particle, their velocities should be evaluated by Equation (31). For cells partially covered by the particle, their velocities are averaged using indicator function given in Equation (39).

The second physical quantity is the force term $\boldsymbol{\lambda}$ in Equation (18). In this work, $\boldsymbol{\lambda}$ is non-zero in particle covered zone and zero elsewhere. It is to enforce the rigid body condition in particle covered zone. In this work, we store this quantity in Eulerian framework. After enforcing rigid body condition using Equation (31), Equation (35) is used to calculate force term $\boldsymbol{\lambda}$ in Eulerian framework in the next time step. Since the particle location is updated at the end of the current time step, resulting in a change in the particle domain, the force term should also be translated with the particle through the following equation

$$\frac{\partial \boldsymbol{\lambda}}{\partial t} + \mathbf{U} \cdot \nabla \boldsymbol{\lambda} = 0 \tag{41}$$

This equation is a pure convection equation, and $\boldsymbol{\lambda}$ remains the same along the characteristic line. Thus, the following scheme is used to solve this equation

$$\lambda(\mathbf{x}, t + \Delta t) = \lambda(\mathbf{x} - \mathbf{U}\Delta t, t) \tag{42}$$

2.4.3 Adjustable time-step for fluid and particle tracking

The flow field of fluid-particle transport in porous media can be quite complex due to interactions among the fluid, particles and pore walls. The radii of the pore channels are not uniform, and the resistance of pore walls on particles depends strongly on pore radius. As a result, the fluid velocity in pores could undergo considerable changes over time. Using a fixed time step may cause

instability problems or high computational cost.

The time step for solving the fluid equations should conform to the CFL (Courant–Friedrichs–Lewy) condition

$$C = \frac{u\Delta t}{\delta} < 1 \tag{43}$$

where C is CFL number preset in the simulation, δ is the cell size and u is the fluid velocity. Based on the preset CFL number, the time step size is adjusted using the following relation

$$(\Delta t)^{n+1} = min\left(min\left(\frac{C}{C_n}, 1.0 + 0.1\frac{C}{C_n}\right), 1.2\right)(\Delta t)^n \tag{44}$$

where C_n is the Courant number at the *n-th* time step. The rate of change in time step is greater when the time step is increased than that when it is reduced. Such a treatment can help to stabilize the numerical simulation.

The time step for particle motion is determined by the collision time in DEM method, and the following relation is adopted

$$\Delta t_p = \frac{\alpha}{s}\sqrt{\frac{m}{k_n}} \tag{45}$$

where α is a constant and α = 0.3 is adopted in this work. s is a half of the number of steps to accomplish one collision, and s = 5 is adopted in this work. m is the mass of the smallest particle in the system. k_n is normal stiffness coefficient in linear DEM model.

It should be stressed that the time step for particle motion and that for continuous phase motion should be coupled. In this work, Equation (44) is adopted as the time step for continuous phase motion, and the time step for particle phase is modified to fit the continuous phase according to

$$\Delta t_p^{corr} = \frac{(\Delta t)^{n+1}}{ceil\left((\Delta t)^{n+1}/\Delta t_p\right)} \tag{46}$$

where Δt_p^{corr} is the time step we adopted in this work for particle motion. The function ceil(x) returns the smallest integer greater than or equal to x.

With the CFD-DNS-DEM coupled method presented here, direct numerical simulation of particle transport in porous media can be simulated at pore scale. The particle cloud can also have a size distribution. However, one should be noted that, if the particle size is much smaller than the pore channel, the point source drag model may be preferred for evaluating fluid-particle force so as to lower computational expense. Moreover, if the particle size is too small, for instance, less than 10 μm, the microscopic forces, such as, Electron double-layer force, Van der Waals force, can have a significant impact on the pore-scale particle cloud behaviors. Incorporating these forces in CFD-DNS-DEM framework for studying the particle cloud behaviors is essential in this situation, but exceeds the scope of the present work.

3 Model Validation

3.1 Flow over a cylinder

Flow over a cylinder is a classical fluid mechanics problem. A large amount of experimental and numerical results have been reported in the literature. In this test case, the simulation domain is 40 d ×20 d (d = 0.025 m), and the center of the cylinder is located at (10 d, 10 d), as shown in Fig. 1. The fluid flows from the left to the right, and the flow velocity is denoted as **u**. The fluid density is ρ_f =1.293 kg·m^{-3} and the kinematic viscosity v=1.5×10^{-5} m^2·s^{-1}. In order to reduce the computational loads, the mesh size of the grid is d/30 × d/30 within the 5 d range of the center line in the flow direction, and the mesh size for the rest is d/5×d/5. The fluid velocity is specified at the inlet and pressure is specified at the outlet. Symmetric plane boundary condition is applied at the top and the bottom walls. Simulations are performed at four different Reynolds numbers, Re (=ρ_f $d|\mathbf{u}|/v$), 10, 20, 40, 100. The corresponding inlet velocities are 6×10^{-4} m·s^{-1}, 1.2×10^{-3} m·s^{-1}, 2.4×10^{-3} m·s^{-1} and 6×10^{-3} m·s^{-1}.

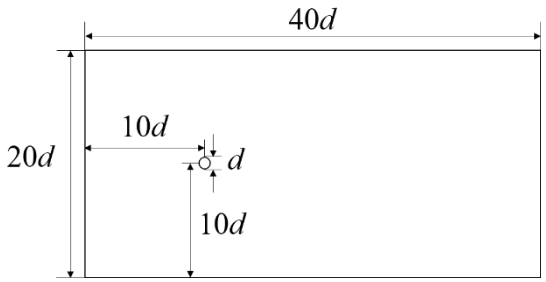

Figure 1 The simulation domain for flow over a cylinder

Table 1 shows the drag coefficient C_d at different Reynolds numbers when the flow field is stable. The drag coefficient is calculated by the following equation

$$C_d = 2|\mathbf{F}^{hyd}|/(\rho_f d|\mathbf{u}|^2) \quad (47)$$

Table 1 give a comparison of mean drag coefficient for different Reynolds numbers between the present results and those in the literature. It can be seen that a good agreement is achieved, showing that the method described here can make a reliable prediction of the fluid-particle interaction force.

Table 1 Comparison of mean drag coefficient for different Reynolds numbers

Re	Su et al.[39]	Silva et al. [40]	Deng et al. [41]	Ranjith Maniyeri [42]	Present
10	-	2.81	2.98	2.98	3.12
20	2.20	2.04	2.06	2.16	2.24
40	1.63	1.54	1.52	1.67	1.67
100	1.40	1.39	1.30	1.32	1.38

3.2 Particle settlement

The settlement process of a circular particle in a closed container is simulated to verify the

feasibility of the method in dealing with moving boundary problems. As shown in Figure 2, the solution domain is 0.02 m × 0.06 m, surrounded by walls. The initial position of the particle is at (0.01 m, 0.04 m), and the particle diameter is $d = 2.5 \times 10^{-3}$ m. Initially, the fluid is at rest and the particle sinks under gravity. The density of the fluid is ρ_f =1000 kg·m^{-3}. The density of the particles ρ_p = 1250 kg·m^{-3} and the dynamic viscosity of the fluid is 0.01 kg·m^{-1}·s^{-1}. The grid size is 0.01 cm × 0.01 cm, and no-slip boundary condition is applied to all walls.

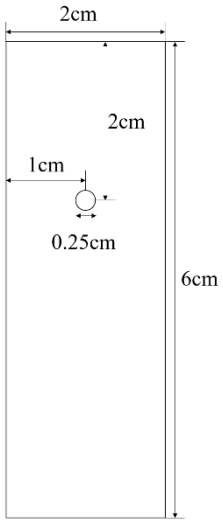

Figure 2 Solution domain and initial particle location for particle settlement

In the early stage, the particle sinks in the fluid under the action of gravity. As the sinking speed increases, the drag force increases gradually. Once gravity force, buoyancy force and drag force reach a balance, sinking velocity remains constant and this velocity is known as particle terminal velocity. The terminal Reynolds number based on terminal velocity is defined as

$$Re_{max} = max\left[\frac{\rho_p d\sqrt{u_p^2(t)+v_p^2(t)}}{\mu}\right] \tag{48}$$

where u_p and v_p are the x and the y components of particle velocity, respectively. This Reynolds number is denoted as terminal Reynolds number from herein.

Table 2 gives the numerical predicted terminal *Re* in this test case along with the results of Wan [43], Glowinski [44] and Wang [45] for comparison. Very small differences can be observed, and our result matches more closely to the result of Wan [43].

Figure 3 gives the evolution of particle sinking velocity and particle vertical position with time. The results of Kang [46] and Glowinski et al. [25] are also included for comparison. It is clear that our predicted particle sinking velocity matches the result of Glowinski et al. very well and is slightly lower than the result of Kang. However, the predicted particle vertical position is not affected by the difference in sinking velocity as a perfect match with the result of Kang can be seen from Fig. 3(b). Glowinski et al. [25] did not report their result on particle vertical position, but a good agreement would be expected given the close match with their predicted particle sinking velocity.

Table 2 The terminal velocity in particle settlement test

	Wan[43]	Glowinski[44]	Wang[45]	This work
Δx/cm	1/96	1/192	1/144	1/100
Re_{max}	17.42	17.27	17.22	17.57

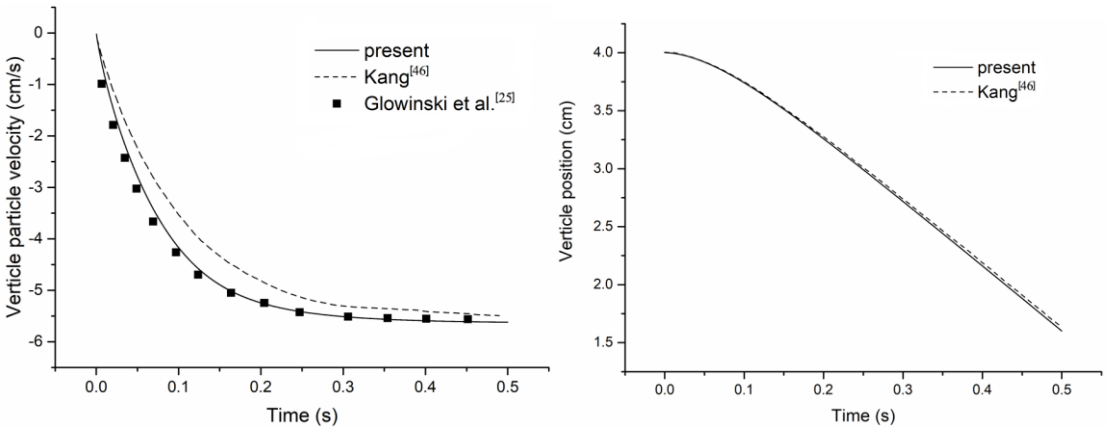

(a) Sinking velocity (b) Verticle position

Figure 3 Sinking velocity and displacement in particle settlement test

4 Pore-scale Simulation of Particle transport in porous media

4.1 Physical Models and Computational conditions

The pore geometry used in the simulation is given in Figure 4. Fluid enters the porous medium from boundary A and exits from boundary B. The physical parameters used in this simulation are given in Table 3. The dimension of the solution is 2. Numerical conditions used in the simulation are shown in Table 4. For pressure, we used Neumann boundary condition for the inlet and wall and Dirichlet for the outlet. For velocity, we used Neumann for outlet and Dirichlet boundary conditions for the inlet. Gamma Scheme presented in work [47] is used to discretize the convection term and Crank-Nicolson scheme is for the time term [48]. Leap-frog scheme is time discretization for particle tracking [49]. To investigate detailed fluid-particle behaviors in the porous medium, six test cases are carried out with different particle counts and particle sizes as given in Table 5. The total particle mass in case IV and that in case V are the same. In all these cases, particles are initially placed at the inlet, and they enter the porous medium through one of the three channels with the fluid and exit when moving to the outlet. Two-phase behaviors in the transport process of fluid-particle system in porous medium are obtained and analyzed in depth.

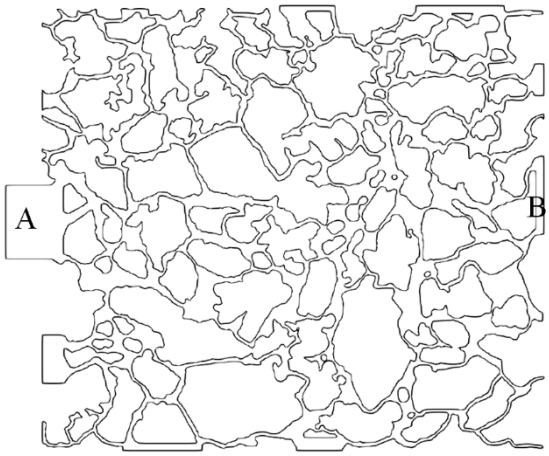

Figure 4 porous structure used in the simulation

Table 3 Physical Parameters used in the simulation

Physical Domain		
Domain Size	0.0103 m × 0.00853 m	
Mesh Count	221743	
Dimension	2	
Fluid Parameters		
Density (ρ_f)	1000	$kg \cdot m^{-3}$
Viscosity (μ)	0.001	$kg \cdot m^{-1} \cdot s^{-1}$
Inlet velocity (**u**)	(0.1, 0, 0)	$m \cdot s^{-1}$
Particle parameters		
Shape	Sphere	
Density(ρ_p)	1000.0	$kg \cdot m^{-3}$
Normal /tangential stiffness (k_n/k_t)	800/200	$N \cdot m^{-1}$
Normal / tangential damping coefficient (η_n/η_t)	0.3/0.3	$N \cdot s \cdot m^{-1}$
Frictional coefficient(χ)	0.1	

Table 4 Numerical parameters used in the simulation

Conditions for continuous phase		
Pressure (p)	Inlet	Neumann
	outlet	Dirichlet
	wall	Neumann
Velocity(**u**)	Inlet	Dirichlet
	outlet	Neumann
	wall	No slip
Particle Phase		
Distance for searching potential particle pair	$2*d_{max}$	
Particle behaviors at outlet	exit	
Particle behaviors at inlet	exit	
Particle behaviors at inlet	Interaction force calculated by DEM	
Numerical scheme		

Convection term	Gamma Scheme
Time scheme for continuous phase	Crank-Nicolson
Time scheme for particle phase	Leap-frog

Table 5 Particle count and diameter in different cases

Cases	Particle Number	Particle Diameter (m)
Case I	1	1.50e-4
Case II	2	1.50e-4
Case III	3	1.50e-4
Case IV	70	1.13e-4
Case V	28	1.90e-4
Case VI	0	not applicable

4.2 Single Particle motion

Figure 5 shows the particle trajectory of a single particle in the porous medium (Case I). It appears that the particle moves along the mainstream direction (from the inlet to the outlet). To understand the particle motion path, the single-phase flow field (Case VI) is presented in Figure 6. It reveals a non-uniform velocity distribution in the porous medium, with fluid motion being limited to a few inter-connected pore channels. Under the action of fluid flow, the particle moves along one of the paths connected by these channels.

Since the radii of the pore channels along the particle moving path are not the same, the acting force of pore walls on the particle are different at different sites. Figure 7 shows the change in pressure-difference between the inlet and outlet over time, where a number of spikes can be seen. Variations in pressure-difference are mainly caused by changes in resistance to the particle during its movement. In order to explain the reasons for causing the spikes in pressure-difference, the corresponding particle locations at the time points of the observed spikes are labelled in Figure 5. Comparing Figure 5 and Figure 7, one can find that the particle is passing through a narrow throat when there is a surge in pressure difference.

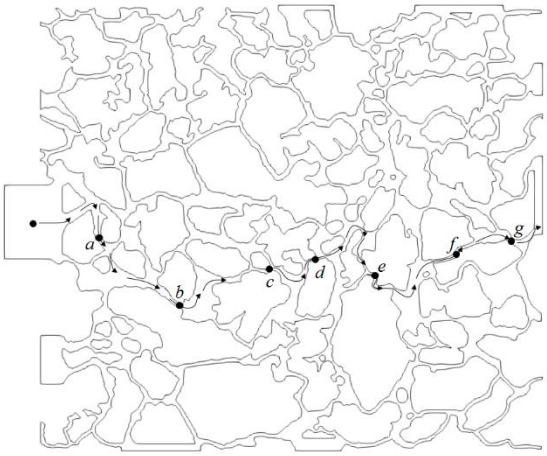

Figure 5 Particle trajectory of a single particle in the porous medium (Case I)

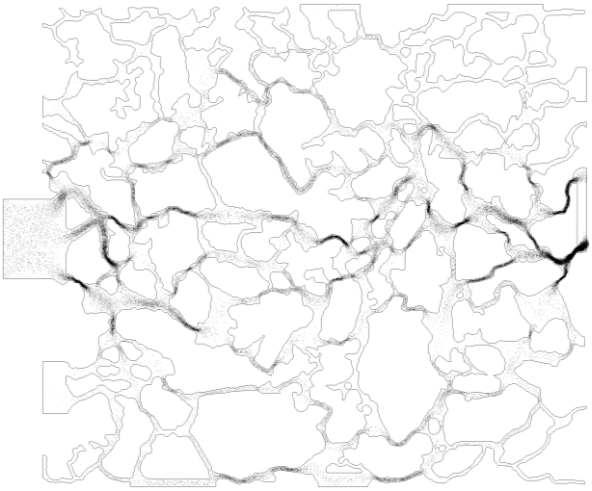

Figure 6 Fluid phase velocity field (Case VI)

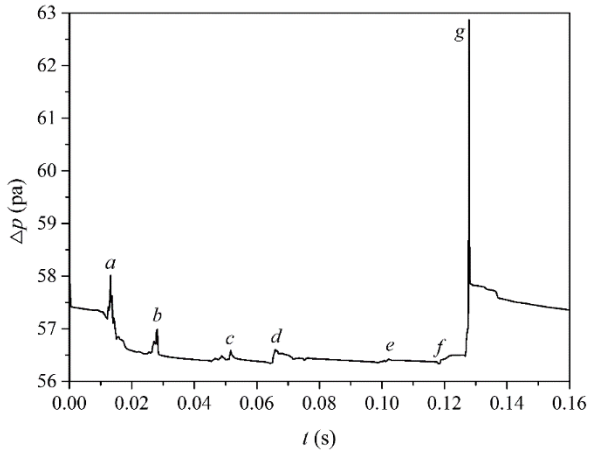

Figure 7 Evolution of pressure-difference between the inlet and outlet with time for single particle transport (Case I)

Comparison of the pore size at point *a* and point *e* in Figure 5 shows that the pore radius at point *a* is larger than that at point *e*. However, the inlet-outlet pressure-difference at point *a* is much larger than that at point *e*. Thus, pore radius is not the only factor influencing the pressure-difference. To explore this further, the single-phase velocity fields near points *a* and *e*, and the flow fields when particle is at point *a* and point *e* are given in Figure 8. When the particle is located at point *a*, channel 1 is temporarily blocked, causing flow velocities in Channel 4, Channel 8 and Channel 9 to increase, and velocities in Channel 2, Channel 3, Channel 5, Channel 6 and Channel 7 to decrease. However, from Figure 8*c* and 8*d*, one can see that blockage of Channel 10 only causes fluid velocity in Channel 11 to reduce, whilst little influence can be noticed on velocities in the other channels. Although the pore radius at point *e* in Channel 10 is smaller than that at point *a* in Channel 1, the pressure-difference is higher when the particle is at point *a* than at point *e* because of the high flow rate. The total flow velocity in channel 1 (marked in Figure 8*b*, point *a* is in this channel) is much higher than in channel 10 (marked in Figure 8*d*, point *e* is located in this channel). Similarly, there is a sharp rise in the inlet-outlet pressure-difference at point *g*, because

the flow rate at this point is very high. If this channel is blocked, all fluid has to exit the solution domain from the other channel, resulting in a high pressure drop.

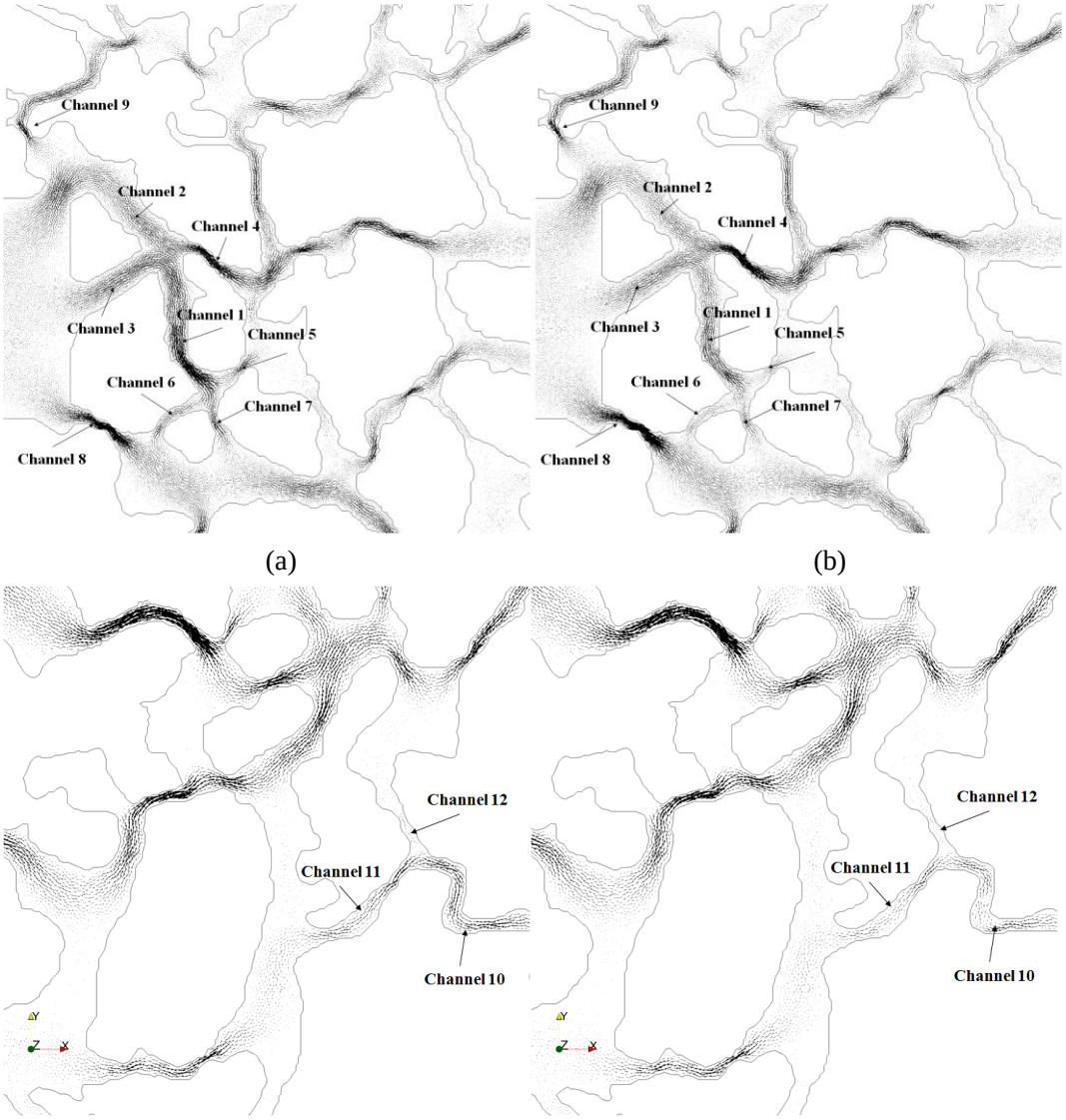

Figure 8 Local velocity fields of single-phase flow and single-particle transport; (a) single phase flow field near point *a* (the location is marked in Figure 5); (b) flow field with particle at point *a*; (c) single-phase flow field near point *e* (the location is marked in Figure 5); (d) flow field with particle at point *e*.

The pressure difference displayed in Figure 7 also reveals small-scale fluctuations in addition to large-scale spikes. To find the reason for this phenomenon, a close-up of the local geometry near point *c* (marked in Figure 5) is given in Figure 9, and the corresponding pressure-difference as the particle moves through this domain is presented in Figure 10. Looking at Figure 9 and Figure 10 together, one can observe that the pressure difference is large when the particle passes through narrow pores, whereas pressure-difference is small when the particle passes through wide pores.

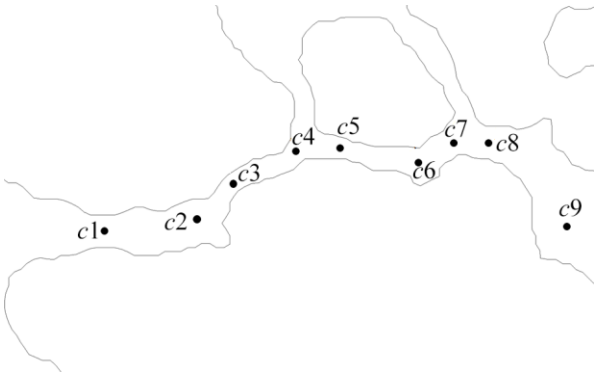

Figure 9 Local geometry near the point c in Figure 5

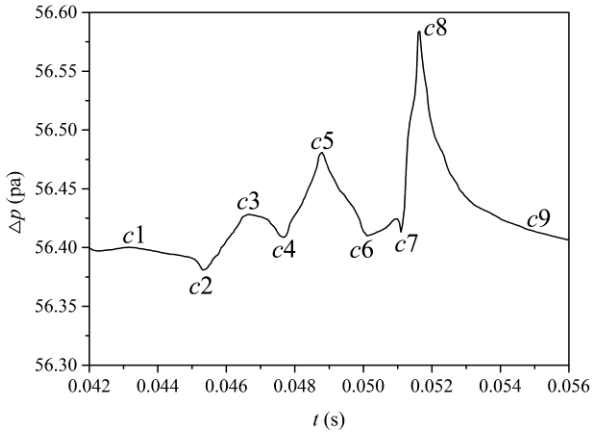

Figure 10 Pressure difference in the process of particle passing through the pore space near point *c* marked in Figure 5

In summary, the inlet-outlet pressure-difference curves show large-scale spikes and small-scale fluctuations for the transport of a single particle in fluid flow. The large-scale spikes are caused by differences in velocity in different channels. If a particle blocks a channel with a high flow-rate, more fluids must bypass this passage to reach the outlet, resulting in a larger pressure difference. Once the particle breaks through the throat in the pore channel, the flow rate in this channel will recover, and the pressure difference falls. For a fixed flow rate, the inlet-outlet pressure difference is controlled by pore radius. Small-scale fluctuations are caused by changes in pore radius in single-particle transport.

4.3 Inter-particle motion interference

In order to investigate fluid-particle behaviors in depth, we have simulated a problem of two-particle transport in a porous medium (Case II). The particle trajectories are shown in Figure 11, along with the evolution of pressure difference between the inlet and outlet given in Figure 12.

Comparing Figures 7 and 12 suggests that the pressure-difference curve in Case II is more complex than that in Case I, and small-scale fluctuations are more obvious. The particle positions in the porous medium at the 9 different time points (*a*-*i*) shown in Figure 12 are marked in Figure

11. A surge in pressure difference tends to coincide with the moment when two channels are blocked by the particles at the same time, showing a "cooperative clogging" feature. The black particle in Case II and the particle in Case I enter the porous medium from the same channel, however, their migration paths are different. As shown in Figure 11, from points *c* to *g* the particle in Case I (single-particle transport) moves along the dotted line, while the black particle in Case II (two particle transport) moves along the solid line. Clearly, the black particle behavior in Case II is interfered by the other particle.

The primary reason for inter-particle motion interference during their migration in porous media is due to variations in pore channel size, resulting in different resistances to particles from the pore wall during the migration process. When a particle (denoted as particle I) moves to a throat, wall resistance on the particle will increase, causing the particle to slow down or even stop; these will reduce the fluid velocity in the channel (denoted as channel I) where particle I is in, thereby increasing the upstream pressure. As a result, fluid velocity in the nearby channels (e.g. channel II) will increase. The particle (denoted as particle II) moving in channel II will also be accelerated due to increase in the fluid drag force (inter-particle motion interference). However, when particle II moves to a throat and becomes stuck there, the upstream pressure will increase even further and the flow behavior of particle I will be affected (secondary interference). The clogging effect of particles changes the local flow field and interferes with the movement of other particles in the affected flow field, which is called inter-particle motion interference in this work. Because of inter-particle motion interference, the particles will produce cooperative clogging behavior, which makes the large-scale pressure difference greater and the small-scale pressure-difference fluctuation more complex for the two-particle transport case than the single particle transport case.

Moreover, particle blocking alters the local fluid field, making the particles show “cooperative motion” feature in a macroscopic view. As can be seen from Figure 12, the time required for the migration of the two particles from the inlet to the outlet is 0.104 s, while the single particle migration time is 0.126 s. This is mainly because when a particle is blocked at a throat, the upstream pressure must increase. As a result, fluid velocity in the nearby channels increases and the particles residing in these channels are accelerated. Once the affected particle moves to a throat, the original blocked particle may be forced to break through the throat and accelerate. Thus, inter-particle interference can mutually enhance particle motion.

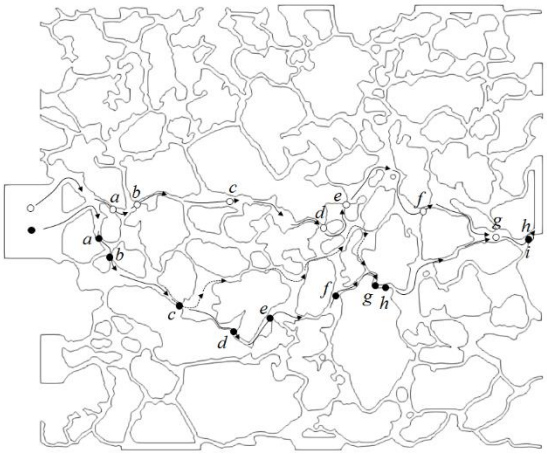

Figure 11 Particle trajectories for two particles transport in a porous medium (Case II)

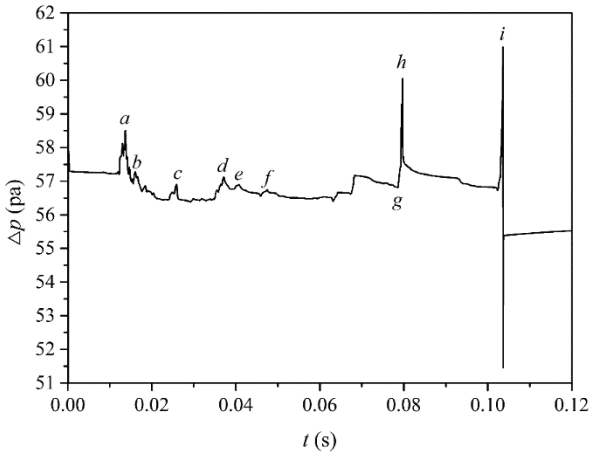

Figure 12 Evolution of Pressure Difference between the inlet and outlet with time for two particles transport (Case II)

Finally, we simulated the motion of three particles in a porous medium (Case III). At the initial time, the three particles are placed at different positions so that they enter the porous medium from different inlets. Particle trajectories are given in Figure 13. Variations of the pressure difference between the inlet and outlet are shown in Figure 14. The pressure difference variations are more complex than those of single-particle or two-particle motions. The white particle and the black particle in this case have the same trajectories as those in Case II. The white particle with a dot is diverted to the non-mainstream region under the action of the fluid; its velocity is lower than the other two particles in the mainstream area, and eventually it is trapped in the porous medium. At the beginning, as the three inlet channels are partially blocked, the pressure difference between the inlet and outlet during the time of 0-0.02 s is larger than that in Case I and Case II. Once the white particle moves to the marginal area of the porous medium, this particle has little influence on the other particles' movement and the characteristics of pressure-difference variation are similar to those in Case II after the time 0.02 s. The migration times of white particle and the black particle in the pores are almost the same as those in Case II.

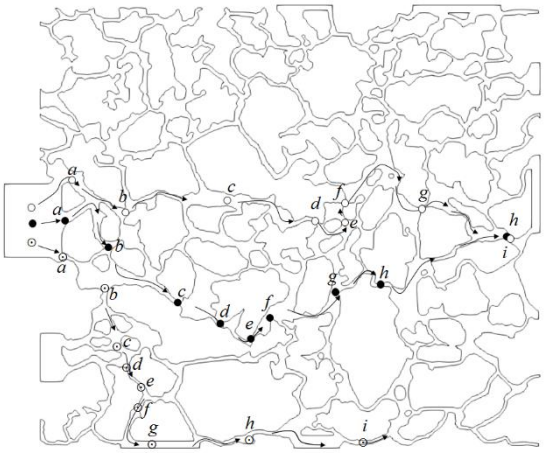

Figure 13 Particle trajectories for three particles transport in a porous medium (Case III)

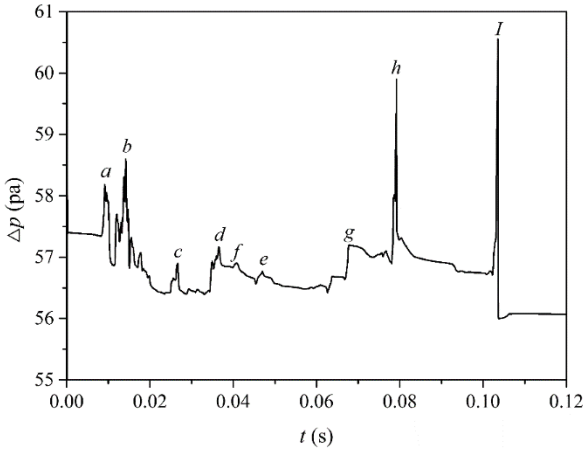

Figure 14 Evolution of Pressure Difference between the inlet and outlet with time for two particles transport (Case III)

4.4 Flow Characteristics of particle cloud

4.4.1 Particle Flow Phenomenon

Figure 15 shows the particle distribution in Case IV at different times, (a) t = 0 s, (b) t = 0.025 s; (c) t = 0.045 s; (d) t = 0.065 s; (e) t =∞(final steady state). The initial particle distribution at the entrance is shown in Figure 15(a). Under the action of the fluid, these particles enter the porous medium from three different channels. Figure 15 (b) gives the particle distribution at 0.025 s. Several particle clusters in the porous medium can be easily observed, such as clusters located at position I (7 particles), II (6 particles), III (5 particles), and IV (12 particles). The main reasons for the local agglomeration of particles are as follows: (1) the pore radii of the channels are different, resulting in different motion resistances to the particles. When the particles move to a throat, the resistance increases to form clogging, this will cause fluid velocity in the channel to decrease and the particles in this channel to accumulate in the upstream region of the throat. Therefore, particle accumulation generally occurs in pores with relatively large channel radius. (2) Collisions between particles are not completely elastic and involve energy losses, making the particles slow down. As

particles migrate deep inside a porous medium, particles from different inlet channels gradually migrate to different pore spaces. As shown in Figure 15 (c), particles entering from the top channel move to zone A, and particles entering from the middle channel move to zone B, whilst particles entering from the lower channel are transported to zone C. Zone B is the mainstream zone, where there is a large pressure gradient and particles are subject to relatively large drag force. Therefore, the average particle velocity in Zone B is greater than that in Zone A and Zone C. As time advances, majority of the particles in the three regions gradually move towards the outlet, as shown in Figure 15 (d), and eventually leave the porous medium. However, several particles are trapped inside the porous medium, as shown in Figure 15 (e), because these particles are not in the main transport channel, and the fluid action on the particles are not sufficient to move them.

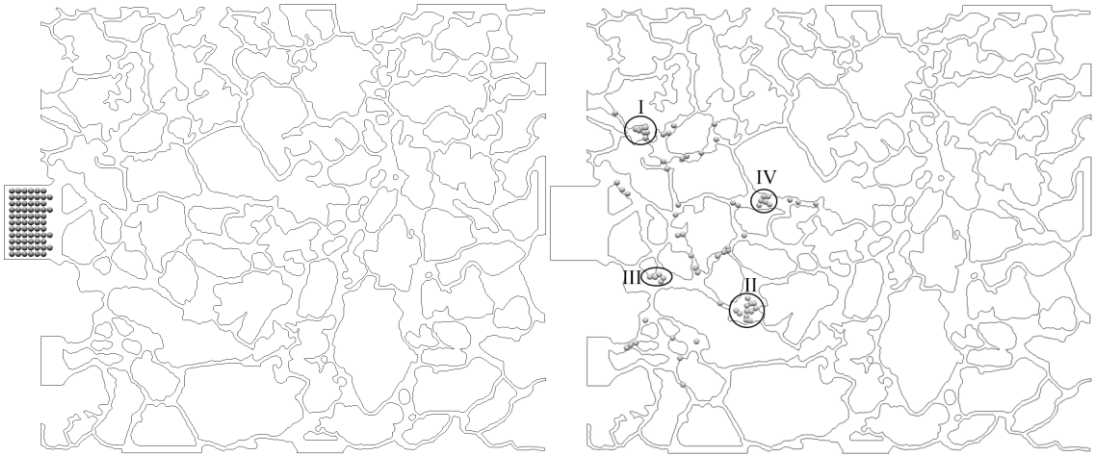

(a) (b)

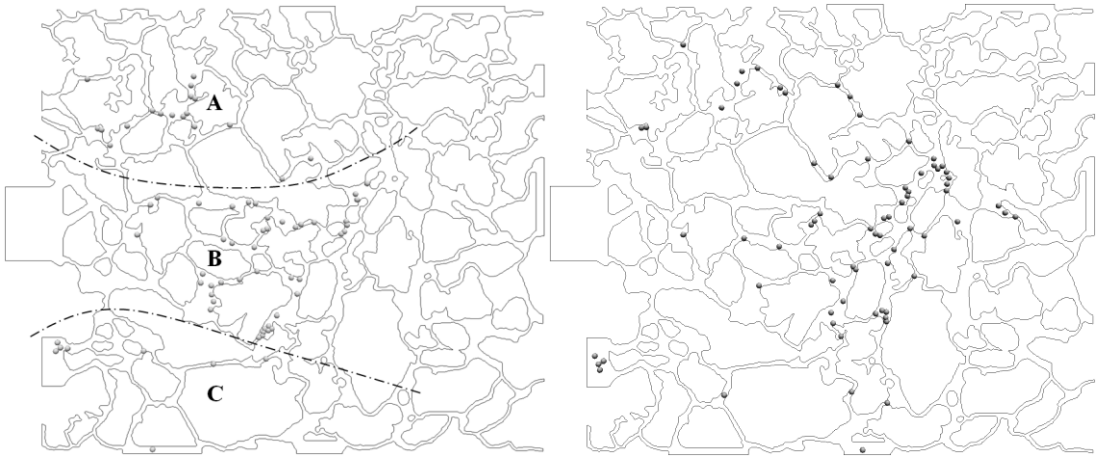

(c) (d)

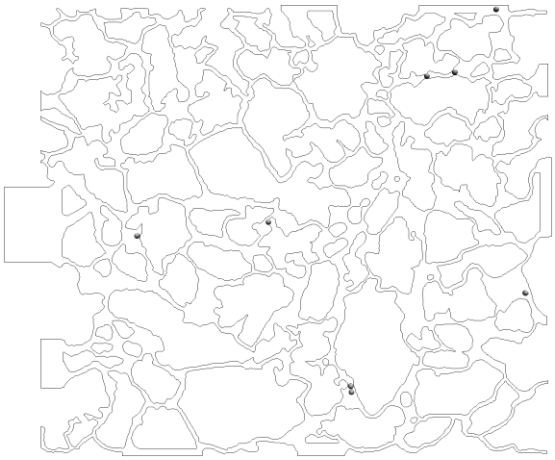

(e)

Figure 15 Particle Distribution at different time points (Case IV)

(a) t = 0 s; (b) t = 0.025 s; (c) t = 0.045 s; (d) t = 0.065 s; (e) $t = \infty$(final steady state);

4.4.2 Pressure Difference Characteristics

Figure 16 shows the pressure-difference variations with time in Case IV and Case V along with those from a single-phase flow simulation with the influence of particle (Case VI) for comparison. Although the total particle mass in Case IV and Case V are the same, they exhibit different pressure-difference variations, suggesting that particle size is an important factor influencing the pressure-difference. Compared with Case IV, Case V has more prominent large spikes and more obvious small-scale fluctuation but at a lower frequency. In single-phase fluid simulation, the inlet-outlet pressure-difference remains constant.

Comparing the pressure-difference variations between the cases with particles and the case without particles, one can find that with particles in the fluid the pressure-difference is higher than that of single-phase fluid flow alone. This is because resistance on a fluid-particle two-phase system is greater than that of a single-phase system. The main source of resistance can be divided into two parts: (1) In the presence of particles, the apparent viscosity of the fluid increases, and this part of resistance is called additional viscous resistance; (2) As the sizes of pore channels are not uniform, when particles clog a throat, the fluid needs to go through a longer path to reach the exit, resulting in a larger resistance. This resistance is called clogging resistance. Additional viscosity is the physical property of a fluid-particle two-phase system, which is usually related to the mass concentration of particles in the system. The pressure difference in Case VI and V (Figure 14) between 0.04 s - 0.07 s shows that the particles do not form an effective clogging (the pressure fluctuation is relatively small) during this period. When the particles enter the porous medium from the entrance, large particles are more likely to form effective clogging. Therefore, the larger particles in Case V are more likely to block the pore channels between 0-0.03 s, resulting in a higher clogging resistance and larger pressure difference than in Case VI.

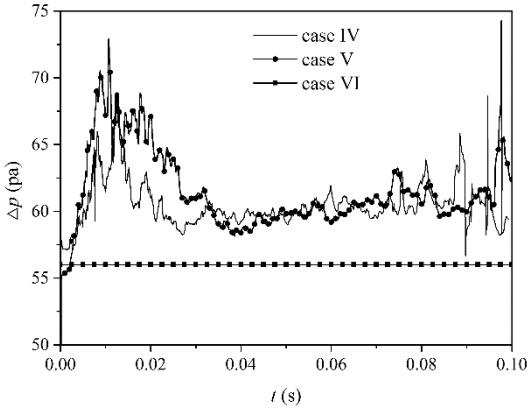

Figure 16 Evolution of pressure difference between inlet and outlet with time for particle cloud

4.4.3 Particle Trajectory

Figure 17 shows the trajectories of all particles in the porous medium in (a) Case VI (b) Case V. It can be seen that only not all channels are used as passages for particles' motion. This is mainly determined by the pore channel structure and pressure conditions. Most of the particles in Case VI move along channels in the mainstream zone (Zone B in figure 15c), while the number of particles passing through channels in the marginal zone (Zone A and C in Figure 15c) is relatively small. Case V has a smaller number of particles passing through channels in the mainstream zone than Case VI, and the particles are more dispersed in space. This is due to the smaller particle size in Case VI and the relatively low damping forces from pore walls. The action of fluid on particles dominates the particle motion, as a result, more particles tend to move in the mainstream zone where fluid velocity is large. On the other hand, the larger particle size in Case V causes larger resistance on these particles, making them more likely to block the throat, diverting the fluid from the mainstream to marginal zones. It is evident from Figure 17 that more channels are involved in transporting particles in Case VI than in Case V.

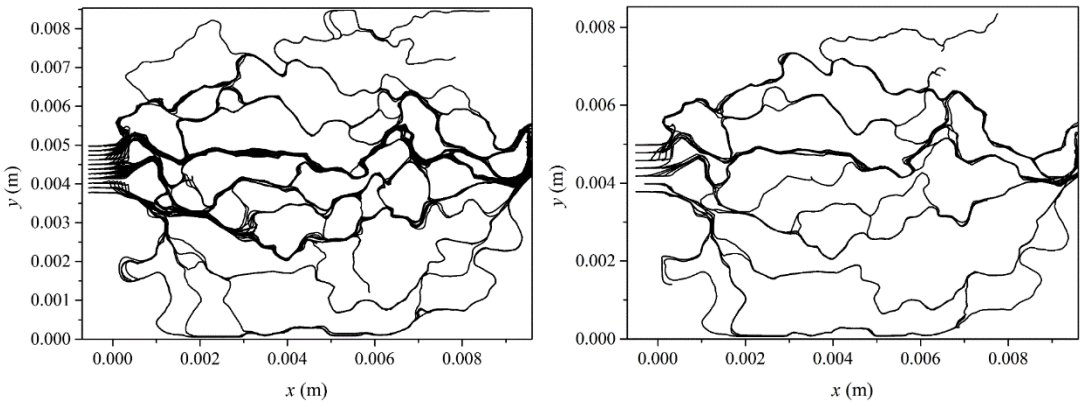

Figure 17 Particle trajectories for particle cloud transport in porous media; (a) Case VI (b) Case V

4.4.4 Particle Macroscopic Motion

In order to investigate the macroscopic migration behaviors of the particle cloud, Figure 18 gives

the average positions in x and y direction in Case IV and V. To study particle dispersion behaviors in the vertical direction, the particles are divided into two groups when calculating average position in the y direction: particles with y coordinates larger than the average y coordinate of all particles belong to the first group, and those with the y coordinate smaller than the average y coordinates belong to the second group. The X and Y values in Figure 18 are calculated by the following equations:

$$X = \frac{\sum_i x_i}{n} \tag{49}$$

$$Y_1 = \frac{\sum_i^{n_1}\left(y_{1i} - \frac{\sum_j^n y_j}{n}\right)}{n_1} \tag{50}$$

$$Y_2 = \frac{\sum_i^{n_2}\left(y_{2i} - \frac{\sum_j^n y_j}{n}\right)}{n_2} \tag{51}$$

where n is the total number of particles, x_i and y_i are the x and y coordinates of particle i. y_{1i} is y coordinates of particle i in group 1 and y_{2i} is that in group 2. n_1 and n_2 are total numbers of particles in the first and the second group, respectively. Because the y coordinates of particles in the first group are larger than the average y coordinate of all particles, Y_1 is always greater than 0. The y coordinates of particles in the second group are less than the average y coordinate of all particles, and thus Y_2 is always less than 0. From Figure 15 (a), the motion of particles in a larger space near the entrance during the period 0 - 0.007 s is almost the same in X direction in both cases. After entering the porous medium, it is obvious that the average velocity of small particles (Case V) in the X direction is larger than that of the large particles (Case IV). This is caused by the fact that in Case VI most of the small particles move along the channels in the mainstream zone, the fluid velocity in this zone is relatively large and the damping forces from pore walls are small. Therefore, small particles have a larger mainstream migration speed. The particle dispersion in the Y direction is shown in Figure 18 (b). It can be seen that large particles have higher migration speed in the longitudinal direction and a better longitudinal distribution. This is mainly because large particles are more likely to be blocked in the mainstream zone, forcing the fluid to flow around the marginal region, thus driving the particles to move to these areas.

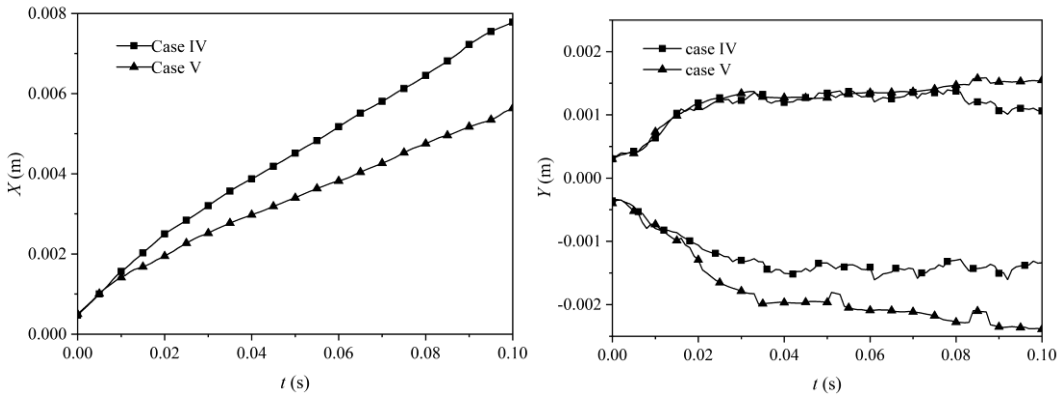

(a) (b)

Figure 18 Average position of all the particles in the simulation; (a) average position in x direction; (b) average position in y directions.

Conclusion

A direct numerical simulation method for fluid particle flow in porous media is presented in this paper. In this method, the Navier-Stokes equation is used to describe the movement of fluid in pores in the Eulerian framework. The discrete element method is used to describe particle-particle contact and particle-wall contact states in the Lagrangian framework. The ERIGID is used to detect the contact between the particles and the pore walls. The fictitious domain method is used to evaluate fluid-particle interactions. The numerical accuracy of the discrete element method is enhanced by the base point-increment method. The time coupling between fluid tracking and discrete element method is realized by a dual adaptive time stepping scheme. Fluid-particle dynamical behaviors in pore space can be easily tracked with our new method. The accuracy and effectiveness of the method are verified by numerical experiments including flow over a cylinder and the settling of a sphere. Finally, the fluid-particle flow process in a porous medium is simulated and our main findings are summarized as follows.

(1) Particle clogging – breakthrough causes local pressure changes, which are reflected through changes in pressure difference between the inlet and outlet. The pressure difference time-variation curve exhibits large-scale spikes and small-scale fluctuations.

(2) Pressure-difference variations as a result of particle clogging -breakthrough can cause the fluid velocity to fluctuate in local pore space, influencing the motion of particles in the affected domain. Particle motion interference exists when multiple particles are moving in the porous medium.

(3) Relative to single-phase fluid flow, the porous medium exerts a higher resistance to a fluid-particle system. The increase in resistance is mainly due to increase in apparent viscosity of the system and the bypass resistance caused by particle clogging.

(4) Particle size plays an important role in the migration and dispersion of particles in porous media. Small particles are more likely to migrate along the direction of the mainstream and less dispersive along the direction perpendicular to flow than large particles.

Acknowledgement

This work is supported by National Science and Technology Major Project (No. 2016ZX05011003) and National Natural Science Foundation of China (No. 21306145).

Reference

[1] Qiu Y, Wu F, Wei M, et al. Lessons Learned from Applying Particle Gels in Mature Oilfields[C]//

SPE Improved Oil Recovery symposium, 12-16 April, Tulsa, Oklahoma 2014.
[2] Mcbride D, Gebhardt J, Croft N, et al. Heap Leaching: Modelling and Forecasting Using CFD Technology[J]. Minerals, 2018, 8(9):1-20.
[3] Nie B, Fan P, Li X. Quantitative investigation of anisotropic characteristics of methane-induced strain in coal based on coal particle tracking method with X-ray computer tomography. Fuel. 2018, 214(15): 272-84.
[4] Papamichos E, Vardoulakis I, Tronvoll J, et al. Volumetric sand production model and experiment[J]. International Journal for Numerical & Analytical Methods in Geomechanics, 2010, 25(8):789-808.
[5]Zamani A, Maini B. Flow of dispersed particles through porous media — Deep bed filtration[J]. Journal of Petroleum Science & Engineering, 2009, 69(1):71-88.
[6] Boccardo G, Marchisio D L, Sethi R. Microscale simulation of particle deposition in porous media.[J]. Journal of Colloid & Interface Science, 2014, 417(3):227-237.
[7] Gitis V, Rubinstein I, Livshits M, et al. Deep-bed filtration model with multistage deposition kinetics[J]. Chemical Engineering Journal, 2010, 163(1):78-85.
[8] Shapiro A A, Bedrikovetsky P G. A stochastic theory for deep bed filtration accounting for dispersion and size distributions[J]. Physica A Statistical Mechanics & Its Applications, 2010, 389(13):2473-2494.
[9] Kleinstreuer C, Yu F, Childress E. Drug-targeting methodologies with applications: A review[J]. World Journal of Clinical Cases, 2014, 2(12):742-756.
[10] Fallah H, Fathi H B, Mohammadi H. The Mathematical Model for Particle Suspension Flow through Porous Medium[J]. Geomaterials, 2012, 2(3):57-62.
[11] Jung J, Cao S C, Shin Y H, et al. A microfluidic pore model to study the migration of fine particles in single-phase and multi-phase flows in porous media[J]. Microsystem Technologies, 2018, 24(2): 1071-1080.
[12] Cundall P A, Strack O D L. A discrete numerical model for granular assemblies[J]. Geothechnique, 1979, 29(30):331-336.
[13] Yang S, Luo K, Fang M, et al. Parallel CFD–DEM modeling of the hydrodynamics in a lab-scale double slot-rectangular spouted bed with a partition plate[J]. Chemical Engineering Journal, 2014, 236(1):158-170.
[14] Yang S, Luo K, Fan J, et al. Particle- scale investigation of the solid dispersion and residence properties in a 3- D spout- fluid bed. AIChE Journal, 2014, 60(8), 2788-2804.
[15] H.P. Zhu, Z.Y. Zhou, R.Y. Yang, et al. Discrete particle simulation of particulate systems: A review of major applications and findings[J]. Chemical Engineering Science, 2008, 62(13):3378-3396.
[16] Zhang H, Li T, Huang Z, et al. Investigation on vertical plug formation of coarse particles in a non-mechanical feeder by CFD-DEM coupling method[J]. Powder Technology, 2018, 332(1):79-89.
[17] Sun R, Xiao H. Diffusion-based coarse graining in hybrid continuum–discrete solvers: Applications in CFD–DEM[J]. International Journal of Multiphase Flow, 2015, 77(23):142-157.
[18] Ge W, Wang L, Xu J, et al. Discrete simulation of granular and particle-fluid flows: from fundamental study to engineering application[J]. Reviews in Chemical Engineering, 2017,

776 33(6):551-623.
777 [19] Su J, Gu Z, Chen C, et al. A two- layer mesh method for discrete element simulation of gas-
778 particle systems with arbitrarily polyhedral mesh[J]. International Journal for Numerical Methods in
779 Engineering, 2015, 103(10):759-780.
780 [20] Xu L, Luo K, Zhao Y, et al. Multiscale investigation of tube erosion in fluidized bed based on
781 CFD-DEM simulation[J]. Chemical Engineering Science, 2018, 183(29):60-74.
782 [21] Su J, Huang C, Gu Z, et al. An Efficient RIGID Algorithm and Its Application to the Simulation of
783 Particle Transport in Porous Medium[J]. Transport in Porous Media, 2016, 114(1):1-33.
784 [22] Su J, Gu Z, Xu XY. Discrete element simulation of particle flow in arbitrarily complex
785 geometries[J]. Chemical Engineering Science, 2011, 66(23):6069-6088.
786 [23] Su J, Gu Z, Zhang M, et al. An improved version of RIGID for discrete element simulation of
787 particle flows with arbitrarily complex geometries[J]. Powder Technology, 2014, 253(2):393-405.
788 [24] Gallier S, Lemaire E, Lobry L, et al. A fictitious domain approach for the simulation of dense
789 suspensions[J]. Journal of Computational Physics, 2014, 256(1):367-387.
790 [25] GLOWINSKI R, PAN T, HESLA T I, et al. A distributed Lagrange multiplier/fictitious domain
791 method for flows around moving rigid bodies: Application to particulate flow[J]. Computer Methods in
792 Applied Mechanics & Engineering, 2015, 30(8):1043-1066.
793 [26] Kempe T, Hlich J. An improved immersed boundary method with direct forcing for the simulation
794 of particle laden flows[J]. Journal of Computational Physics, 2012, 231(9): 3663-3684.
795 [27] Markus Uhlmann. An immersed boundary method with direct forcing for the simulation of
796 particulate flows[J]. Journal of Computational Physics, 2005, 209(2): 448-476.
797 [28] Lu J, Das S, Peters E A J F, et al. Direct Numerical Simulation of Fluid Flow and Mass Transfer in
798 Dense Fluid-particle Systems with Surface Reactions[J]. Chemical Engineering Science, 2018, 81(1):
799 329-244.
800 [29] Pantokratoras A. Direct Numerical Simulation of Fluid Flow and Mass Transfer in Dense Fluid–
801 Particle Systems[J]. Industrial & Engineering Chemistry Research, 2013, 52(33):11266-11274.
802 [30] Macpherson, G.B., Nordin, N., Weller, H.G.: Particle tracking in unstructured, arbitrary
803 polyhedral meshes for use in CFD and molecular dynamics. Commun. Numer. Methods Eng. 2009,
804 25(3): 263–273.
805 [31] Kuang S B, Yu A B, Zou Z S. A new point-locating algorithm under three-dimensional hybrid
806 meshes[J]. International Journal of Multiphase Flow, 2008, 34(11):1023-1030.
807 [32] Chen H, Zhang Y X, Zang M, et al. An accurate and robust contact detection algorithm for
808 particle- solid interaction in combined finite- discrete element analysis[J]. International Journal for
809 Numerical Methods in Engineering, 2015, 103(8):598-624.
810 [33] Shigeto Y, Sakai M. Arbitrary-shaped wall boundary modeling based on signed distance functions
811 for granular flow simulations[J]. Chemical Engineering Journal, 2013, 231(9):464-476.
812 [34] Y. Tsuji, T. Tanaka, T. Ishida. Lagrangian numerical simulation of plug flow of cohesionless
813 particles in a horizontal pipe[J]. Powder Technology, 1992, 71(3):239-250.
814 [35] Munjiza A, Andrews K R F. NBS contact detection algorithm for bodies of similar size[J].
815 International Journal for Numerical Methods in Engineering, 2015, 43(1):131-149.

[36] www.openfoam.org
[37] Issa R I. Solution of the implicitly discretised fluid flow equations by operator-splitting[J]. Journal of Computational Physics, 1991, 62(1):40-65.
[38] Rhie, C. M., Chow, W. L. Numerical study of the turbulent flow past an airfoil with trailing edge separation. AIAA Journal, 1983, 21(11): 1525-1532.
[39] Su S W, Lai M C, Lin C A. An immersed boundary technique for simulating complex flows with rigid boundary[J]. Computers & Fluids, 2007, 36(2):313-324.
[40] Silva A L F L E, Silveira-Neto A, Damasceno J J R. Numerical simulation of two-dimensional flows over a circular cylinder using the immersed boundary method[J]. Journal of Computational Physics, 2003, 189(2):351-370.
[41] Deng J, Shao X M, Ren A L. A new modification of the immersed‐boundary method for simulating flows with complex moving boundaries[J]. International Journal for Numerical Methods in Fluids, 2006, 52(11):1195-1213.
[42] Maniyeri R. Numerical Study of Flow Over a Cylinder Using an Immersed Boundary Finite Volume Method[J]. International Journal of Engineering Research, 2014, 3(4):213-216.
[43] Wan D, Turek S. An efficient multigrid-FEM method for the simulation of solid-liquid two phase flows[J]. Journal of Computational & Applied Mathematics, 2007, 203(2):561-580.
[44] Glowinskia R, Pana T W, Heslab T I, et al. A Fictitious Domain Approach to the Direct Numerical Simulation of Incompressible Viscous Flow Past Moving Rigid Bodies: Application to Particulate Flow[J]. J.comput.phys, 2001, 169(2):363-426.
[45] Wang Z, Fan J, Luo K. Combined multi-direct forcing and immersed boundary method for simulating flows with moving particles[J]. International Journal of Multiphase Flow, 2008, 34(3):283-302.
[46] Kang S K. Immersed boundary methods in the lattice Boltzmann equation for flow simulation[D]. Dissertations & Theses - Gradworks, 2010.
[47] Jasak H, Weller H G, Gosman A D. High resolution NVD differencing scheme for arbitrarily unstructured meshes[J]. International Journal for Numerical Methods in Fluids, 1999, 31(2):431-449.
[48] Crank J, Phyllis N. A practical method for numerical evaluation of solutions of partial differential equations of the heat-conduction type. Mathematical Proceedings of the Cambridge Philosophical Society. 1947, 43(1):50-67.
[49] Rougier E , Munjiza A , John N W M . Numerical comparison of some explicit time integration schemes used in DEM, FEM/DEM and molecular dynamics[J]. International Journal for Numerical Methods in Engineering, 2004, 61(6):856-879.